Energy Level Modification in Lead Sulfide Quantum Dot Thin Films through Ligand Exchange

Patrick R. Brown,[†,▽] Donghun Kim,[‡,▽] Richard R. Lunt,[§] Ni Zhao,[⊥] Moungi G. Bawendi,[‖] Jeffrey C. Grossman,[‡,*] and Vladimir Bulović[#,*]

[†]Department of Physics, Massachusetts Institute of Technology, Cambridge, Massachusetts 02139, United States, [‡]Department of Materials Science and Engineering, Massachusetts Institute of Technology, Cambridge, Massachusetts 02139, United States, [§]Department of Chemical Engineering and Materials Science, Michigan State University, East Lansing, Michigan 48824, United States, [⊥]Department of Electronic Engineering, Chinese University of Hong Kong, Shatin, Hong Kong, [‖]Department of Chemistry, Massachusetts Institute of Technology, Cambridge, Massachusetts 02139, United States, and [#]Department of Electrical Engineering and Computer Science, Massachusetts Institute of Technology, Cambridge, Massachusetts 02139, United States. [▽]These authors contributed equally to this work.

ABSTRACT The electronic properties of colloidal quantum dots (QDs) are critically dependent on both QD size and surface chemistry. Modification of quantum confinement provides control of the QD bandgap, while ligand-induced surface dipoles present a hitherto underutilized means of control over the absolute energy levels of QDs within electronic devices. Here, we show that the energy levels of lead sulfide QDs, measured by ultraviolet photoelectron spectroscopy, shift by up to 0.9 eV between different chemical ligand treatments. The directions of these energy shifts match the results of atomistic density functional theory simulations and scale with the ligand dipole moment. Trends in the performance of photovoltaic devices employing ligand-modified QD films are consistent with the measured energy level shifts. These results identify surface-chemistry-mediated energy level shifts as a means of predictably controlling the electronic properties of colloidal QD films and as a versatile adjustable parameter in the performance optimization of QD optoelectronic devices.

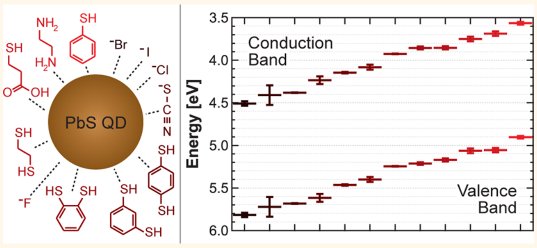

KEYWORDS: lead sulfide · ligands · quantum dots · nanocrystals · ultraviolet photoelectron spectroscopy · density functional theory · solar cells · photovoltaics

Colloidal quantum dots (QDs) possess a uniquely tunable set of electronic properties that has generated considerable interest in their use as active materials in solution-processed photovoltaics.[1] Synthetic techniques allowing reproducible control of QD size enable the preparation of strongly confined lead sulfide (PbS) colloidal QDs with bandgaps ranging from 0.7 to 2.1 eV, spanning the ideal range for single- and multijunction photovoltaic device applications.[2] In complement to the control over the QD bandgap afforded by modification of the nanocrystal size, the electronic properties of coupled colloidal QD solids can also be tuned through modification of the QD surface chemistry *via* ligand exchange.[3] A wide variety of ligand chemistries have been utilized for PbS QDs, the highest-performance QD solar cell material to date,[4] including bidentate aliphatic and aromatic thiols,[5] primary amines,[3] carboxylic acids,[6] thiocyanate ions,[7] and halide ions.[8] For a given ligand, the different facets of the rock-salt-structure PbS nanocrystals present additional differences in steric opportunities and affinities for ligand binding.[9]

Ligand exchange can influence the carrier mobility by changing the inter-QD dielectric environment and tunneling distance; in the absence of other changes, mobility increases exponentially with decreasing ligand length.[10] Appropriate ligands can also passivate electronic trap sites on the QD surface arising from structural aperiodicity and off-stoichiometry of the QD core, increasing carrier and exciton lifetimes and providing a degree of control over the doping level and type of the coupled QD film.[11−13] Changing the identity of the chemical binding group and dipole moment of the ligand should also change the strength of the QD-ligand surface dipole, shifting the

* Address correspondence to
bulovic@mit.edu,
jcg@mit.edu.

Received for review February 13, 2014
and accepted May 13, 2014.

10.1021/nn500897c

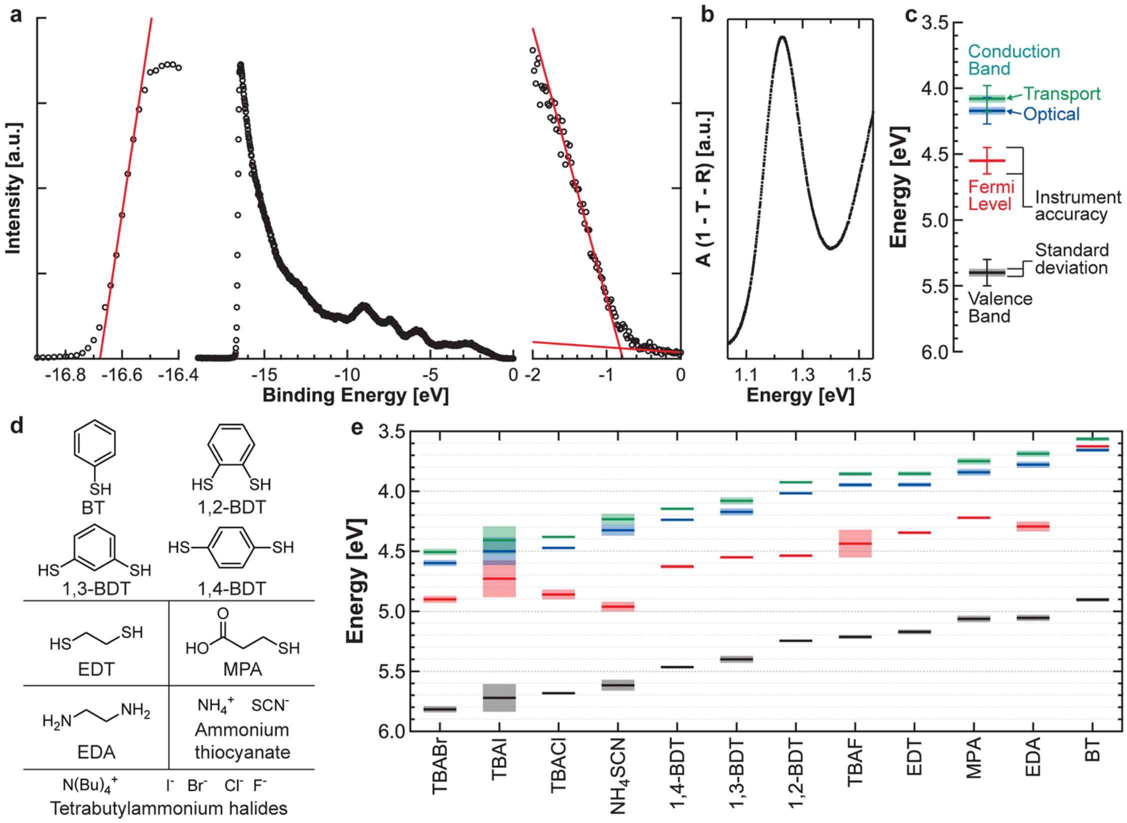

Figure 1. Ligand-dependent energy levels measured by UPS. (a) Complete ultraviolet photoelectron spectrum of 100 nm thick 1,3-BDT-exchanged PbS QD film on gold. The left and right side panels display magnified views of the high-binding-energy cutoff (Fermi level) and low-binding-energy cutoff (valence band edge binding energy) regions, respectively, where the band energies are determined from the intersection of a linear extrapolation from the cutoff region to the baseline. (b) Optical absorption spectrum (absorption = 1 − transmission − reflection) of the first excitonic peak of 1,3-BDT-exchanged PbS QDs. The peak absorption at $E = 1.23$ eV is taken as the optical bandgap. (c) Energy level diagram of 1,3-BDT-exchanged PbS QDs determined from the spectra in (a), (b), and eq 1. Distinction is made between the instrumental accuracy (0.1 eV) and the standard deviation (0.02 eV) across multiple measurements. (d) Chemical structures of the ligands employed in this study. (e) Complete energy level diagrams of PbS QDs exchanged with the ligands shown in d. All PbS QDs used in this figure have a first excitonic absorption peak at $\lambda = 963$ nm in solution with native oleic acid ligands. Each data point represents the average of 2−4 measurements across different samples; shaded bars indicate one standard deviation, and error bars for instrument accuracy are omitted for clarity.

vacuum energy and, in turn, the QD valence band maximum (VBM) and conduction band minimum (CBM). A number of studies have examined the influence of surface chemistry on QD energy levels;[14−17] however, most energy-level studies performed on PbS QDs have been performed on QDs with oleic acid ligands that are too insulating for use in photovoltaic devices,[16,18] or on QDs with a narrow subset of other ligands.[19−21] Given the large shifts in energy levels observed for other species of QDs following ligand exchange, it is unlikely that the energy levels of oleic acid-capped PbS QDs are representative of the energy levels of the ligand-exchanged films used in PbS QD solar cells.

Here, the energy level shifts of PbS QDs treated with 12 different ligands are measured using ultraviolet photoelectron spectroscopy (UPS). The measured valence band maxima span a range of 0.9 eV. Atomistic simulations of the vacuum energy shift induced by the binding of five of these different ligands to pristine PbS slabs reproduce the observed trend in energy level modification. The impact of these energy level shifts on photovoltaic performance is determined through studies on devices employing 1,2-ethanedithiol (EDT), 1,2-benzenedithiol (1,2-BDT), and 1,3-benzenedithiol (1,3-BDT) ligands. Even between these chemically similar ligands, shifts in the VBM of more than 0.2 eV necessitate ligand-dependent adjustments of the electron- and hole-extracting contacts to achieve optimal performance. These results have recently guided the design and understanding of a certified 8.55% efficient PbS QD solar cell, a current record for this class of devices.[22] These findings complement the known tunability of QD bandgap and highlight an important mechanism of control over the electronic properties of colloidal QDs.

RESULTS AND DISCUSSION

Ligand-Dependence of QD Energy Levels Measured by UPS. Figure 1a shows a representative UPS spectrum of a

100 nm thick PbS QD film treated with 1,3-BDT without exposure to air. UPS measures occupied electronic states and thus provides information on the Fermi level (low-binding-energy cutoff) and VBM (high-binding-energy-cutoff) of a material. The energy E_C of the CBM can be approximated by adding the electronic transport gap E_g of the material to the VBM, where E_g is determined from the sum of the optical bandgap E_g^{opt} and the Coulombic stabilization energy of the confined electron and hole, first derived by Brus using the particle-in-a-box model, such that

$$E_C = E_V - E_g = E_V - E_g^{opt} - 1.786\frac{e^2}{4\pi\varepsilon_0\varepsilon_{QD}R} \qquad (1)$$

where e is the charge of the electron, ε_0 is the permittivity of free space, ε_{QD} is the optical dielectric constant of the QD core material, and R is the quantum dot radius (determined by matching the first absorption peak in solution to a published sizing curve).[16,23] The PbS QDs used in this study are highly confined, with quantum-confined bandgaps 0.6−1.1 eV larger than the bulk bandgap of PbS. The confined electrons and holes therefore have a high kinetic energy, and the optical dielectric constant ($\varepsilon_\infty^{PbS} = 17.2$) is a more suitable choice than the static dielectric constant ($\varepsilon_0^{PbS} = 169$).[24]

Figure 1b shows a representative absorption spectrum of 1,3-BDT-treated PbS QDs on glass. The first absorption peak of the solid-state ligand-exchanged QDs is at energy $E_g^{opt} = 1.23$ eV, corresponding to a transport bandgap of $E_g = 1.32$ eV. Figure 1c summarizes the energies of the VBM, Fermi level, and CBM determined from the measurements in Figure 1a,b for 1,3-BDT-treated PbS QDs. While the instrumental accuracy of UPS is ∼0.1 eV,[25] the standard deviation of our measurement (here across 4 different samples) is much smaller, in the range of 0.02 eV.

Figure 1d shows the chemical structure of the 12 ligands employed in this study, including thiols [benzenethiol (BT), 1,2-, 1,3-, and 1,4-benzenedithiol (1,2-BDT, 1,3-BDT, and 1,4-BDT), 1,2-ethanedithiol (EDT), and 3-mercaptopropionic acid (MPA)], a primary amine [1,2-ethylenediamine (EDA)], ammonium thiocyanate (SCN), and halides [tetrabutylammonium iodide (TBAI), bromide (TBABr), chloride (TBACl), and fluoride (TBAF)]. Figure 1e shows the measured energy levels of a single batch of PbS QDs ($\lambda = 963$ nm absorption peak in solution) exchanged with these different ligands, sorted by decreasing VBM binding energy (complete photoemission and absorption spectra are given in the Supporting Information).

A maximum shift of 0.9 eV in the VBM is observed between QDs treated with TBABr and BT. Even among the chemically similar bidentate thiols, a shift of 0.3 eV is observed between PbS QDs treated with EDT and 1,4-BDT. Similarly large shifts in energy levels have been observed for conductors treated with thin layers of amine-containing polymers.[26] Such large shifts are expected to have considerable influence on the operation of electronic devices fabricated using PbS QDs. We note that these energy levels are characteristic only of the specific size of PbS QDs studied here, and only under air-free fabrication and storage conditions; UPS measurements performed on PbS QD films fabricated in air indicate different values for the Fermi level and VBM.[22] It is also notable that the majority of ligands tested in this study give rise to VBMs significantly deeper than those reported for oleic-acid-capped PbS QDs in the literature (oleic acid ligands are too insulating to be employed in UPS, which requires adequate grounding of the emissive surface to prevent charging-induced shifts in the observed energy levels).[16,18] This result highlights the importance of performing energy level measurements on QDs in a chemical environment that is as close as possible to the environment present in an operating device, taking into account both the solid-state ligand environment and the history of exposure to air, vacuum, and solvents.

Ligand Binding Simulations by Density Functional Theory. First-principles density functional theory (DFT) calculations provide insight into the origin of the band energy shifts measured by UPS. DFT calculations are widely used to simulate energy level shifts at interfaces between inorganic materials and organic molecules.[9,11,13,27,28] As shown in Figure 2a, the surface of a PbS QD is approximated as a semi-infinite PbS (100) slab, as the (100) and (111) facets are known to be dominant for PbS QDs (similar trends in DFT results are obtained for binding to Pb-rich (111) facets, as shown in the Supporting Information).[9,29,30] Modeling the QD surface as a semi-infinite quasi-two-dimensional slab is much more computationally efficient than modeling the entire three-dimensional QD/ligand system, and the electrostatic environment encountered by the electron or hole during transfer across the QD/ligand interface should be similar in both cases. A small dependence on the magnitude of the ligand-induced shift on QD size has been observed elsewhere for InAs QDs,[14] but the direction of the trend in energy levels for different ligands is expected to be independent of QD size. As shown in Figure 2a, one side of the slab is passivated by ligands and one side by pseudohydrogen atoms for charge balance. Similar results are obtained when both sides of the slab are passivated by ligands (Figure S10 in the Supporting Information).

Five of the ligands employed above are simulated by DFT (BT, 1,2-BDT, 1,3-BDT, 1,4-BDT, and iodide), with the ligand coverage held constant at one ligand binding group per surface Pb atom (thus BT and iodide have twice the density of the benzenedithiols). The ligands tested here are known to efficiently displace the original oleic acid ligands,[8,31−34] but it is possible that some oleic acid remains bound to the QD surface, perhaps as a result of variations in binding affinity between the (100)

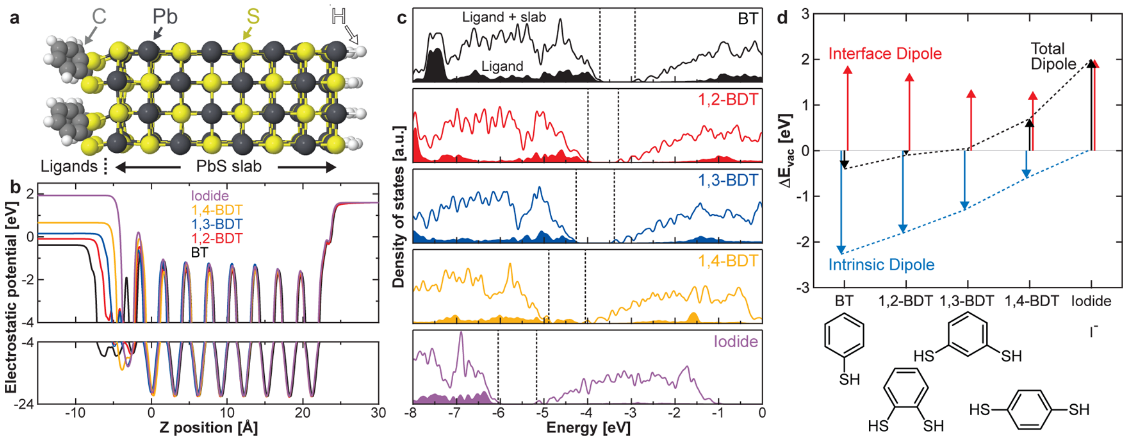

Figure 2. DFT calculations of ligand-induced energy shifts for PbS slabs. (a) Schematic diagram of modeled PbS slab. The left side of the slab is passivated by adsorbed ligands (1,2-BDT is shown here as an example), and the right side is passivated by appropriate pseudohydrogen atoms to ensure charge balance. Monodentate (BT, iodide) and bidentate (1,2-, 1,3-, and 1,4-BDT) ligands are employed here, with ligand density set at one binding atom per surface Pb atom (hence bidentate ligands have half the areal density of monodentate ligands). (b) Plane-averaged electrostatic potentials of PbS slabs with different ligands. The potential in the vacuum region far to the left of an unpassivated PbS slab is set to zero. (c) Density of states of the ligand (filled curve) and ligand-slab system (unfilled curve) for each of the five ligands considered. The vacuum level above each passivated PbS slab is set to zero. The vertical dashed lines signify the valence and conduction band edge energies. (d) Vacuum energy shifts (ΔE_{vac}, black arrows) for each ligand and decomposition into interface ($\Delta E_{\mathrm{vac},1}$, red arrows) and intrinsic ligand ($\Delta E_{\mathrm{vac},2}$, blue arrows) dipoles.

and (111) facets.[9,35,36] To facilitate comparison between the different ligands and simplify the DFT simulations, complete exchange of oleic acid is assumed.

Figure 2b shows the plane-averaged electrostatic potentials for these five ligands bound to PbS (100) slabs. Large shifts in vacuum energy level (ΔE_{vac}) compared to the unpassivated PbS slab are observed. Figure 2c shows the electronic density of states of the ligand (filled curve) and ligand-slab system (unfilled curve) for each of the five ligands. The PbS bandgap remains relatively unchanged upon ligand adsorption, while the VBM and CBM shifts match the ΔE_{vac} observed in Figure 2b, indicating that the band edge shifts are electrostatic in origin. There is excellent agreement in the direction and ordering of band edge shifts observed by UPS and DFT, although the magnitude of the shifts is overestimated by DFT.

Shifts in the energy levels of QDs upon ligand adsorption can be conceptualized as the sum of two dipole contributions: a contribution from the dipole formed between the surface atom of the QD and the binding group of the ligand (here referred to as μ_1), and a contribution from the intrinsic dipole moment of the ligand itself (μ_2).[28] For the Lewis-basic ligands studied here, μ_1 points from the negatively charged ligand to the positively charged lead atom; μ_2 depends on the chemical structure and binding orientation of the ligand. The z-component of the total dipole ($\mu_{\mathrm{total},z}$) can be expressed as $\mu_{\mathrm{total},z} = \mu_{1,z} + \mu_{2,z}$, to which ΔE_{vac} is related through the Helmholtz equation:

$$\Delta E_{\mathrm{vac}} = -\frac{\mu_{\mathrm{total},z}}{A\varepsilon_r\varepsilon_0} = -\left(\frac{\mu_{1,z}}{A\varepsilon_r\varepsilon_0} + \frac{\mu_{2,z}}{A\varepsilon_r\varepsilon_0}\right)$$
$$= \Delta E_{\mathrm{vac},1} + \Delta E_{\mathrm{vac},2} \qquad (2)$$

where A is the surface area of the ligand and ε_r is the dielectric constant of the ligand layer.[27,37−39]

Figure 2d shows ΔE_{vac} for each ligand and the decomposition of ΔE_{vac} into the opposing $\Delta E_{\mathrm{vac},1}$ and $\Delta E_{\mathrm{vac},2}$ terms. The ligand-intrinsic $\Delta E_{\mathrm{vac},2}$ terms follow trends predicted by simple electrostatics: iodide lacks an intrinsic dipole, while $\Delta E_{\mathrm{vac},2}$ for the thiols increases as the angle between C−S bonds decreases. The interfacial $\Delta E_{\mathrm{vac},1}$ term is large for the compact iodide and BT ligands and decreases for more sterically bulky ligands. The trend in ΔE_{vac} is dominated by the influence of the ligand dipole moment rather than the interfacial dipole, as ΔE_{vac} increases monotonically with decreasing $|\Delta E_{\mathrm{vac},2}|$. The lack of an intrinsic dipole moment in opposition to the surface-ligand dipole moment is a general feature of the halide ligands and explains the large band energy shifts observed for this class of ligands in Figure 1e. The excellent agreement across multiple ligand classes with the trends observed in Figure 1e lends support both to the use of UPS to reliably measure QD energy levels and to the intuitive description of energy level shifts presented here.

Ligand-Dependent Photovoltaic Performance. To determine the importance of these shifts in QD energy levels for photovoltaic devices, PbS QDs exchanged with EDT, 1,2-BDT, and 1,3-BDT are incorporated into ZnO/PbS QD np heterojunction,[40] Schottky junction,[41] and donor−acceptor heterojunction[42] photovoltaics. These ligands have been well studied in PbS QD optoelectronic devices to date[5,43,44] and employ identical, reproducible ligand-exchange procedures, so they provide an ideal platform for comparison. All QD film preparation for the photovoltaics studied here is

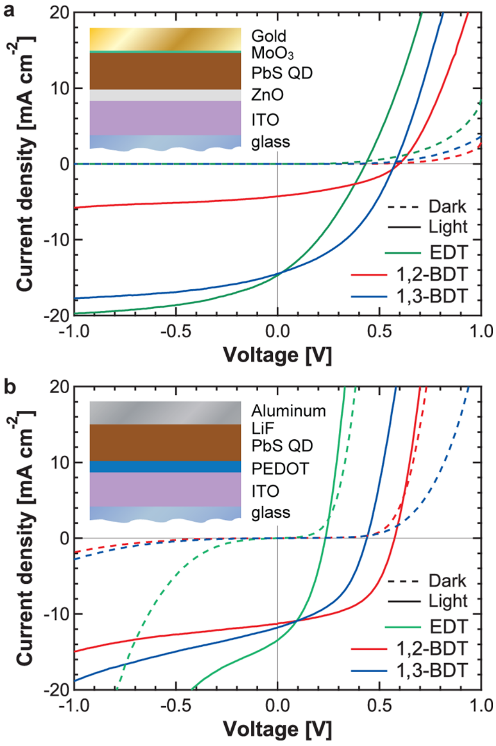

Figure 3. Architecture-dependent photovoltaic performance. Current–voltage characteristics measured in the dark (dashed lines) and under 100 mW cm^{-2} AM1.5 illumination (solid lines) for EDT-, 1,2-BDT-, and 1,3-BDT-exchanged PbS QDs (λ = 905 nm first absorption peak in solution) in (a) ZnO/PbS np-heterojunction and (b) Schottky junction architectures.

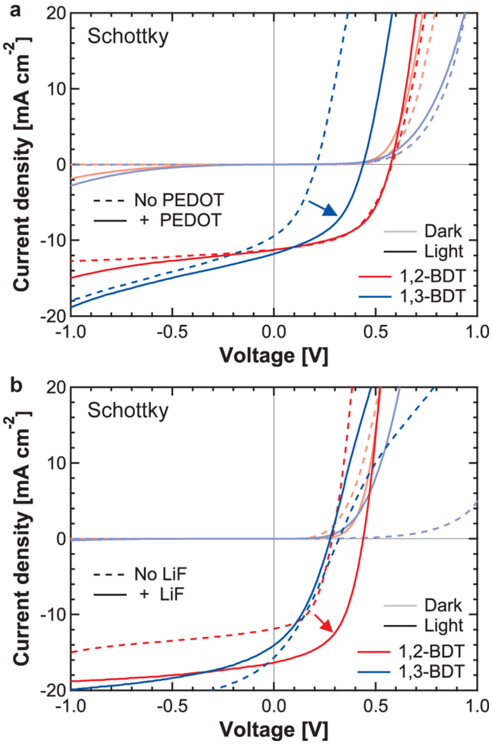

Figure 4. Ligand-induced changes in Schottky photovoltaic performance. (a and b) Current–voltage characteristics of Schottky junction photovoltaics employing 1,2-BDT (red traces) and 1,3-BDT (blue traces) showing the influence of a PEDOT:PSS hole transport layer (a) and a LiF cathode interlayer (b). In each case, the interlayer significantly improves the performance of only one of the two ligands, in a manner in keeping with the results of Figure 1.

performed under the same air- and water-free conditions as the film preparation for the UPS studies described above.

Figure 3 shows the dark and light *J*–*V* characteristics of indium tin oxide (ITO)/ZnO/PbS QD/MoO$_3$/Au np-heterojunction (np-HJ) photovoltaics (Figure 2a) and ITO/Polyethylenedioxythiophene:polystyrene sulfonate (PEDOT:PSS)/PbS QD/LiF/Al Schottky junction (SJ) photovoltaics (Figure 2b) fabricated with EDT-, 1,2-BDT, and 1,3-BDT-exchanged PbS QD (λ = 905 nm first absorption peak in solution) films. Two general performance trends are apparent. First, treatment with EDT results in a lower open-circuit voltage (V_{OC}) than treatment with 1,2-BDT and 1,3-BDT in both the np-HJ and SJ architectures. Second, the relative performance of 1,2-BDT and 1,3-BDT-exchanged QDs is reversed between the np-HJ and SJ architectures: 1,3-BDT exchange results in the best performance for the np-HJ architecture, while 1,2-BDT exchange results in the best performance for the SJ architecture. A straightforward comparison of trap distributions, carrier mobilities, and recombination rates could explain the first of these two trends, but not the second. As described in detail in the Supporting Information, while treatment with EDT leads to the highest carrier mobility of the three ligands studied, the high recombination rate and high trap density of EDT-treated PbS QD films lead to a lower V_{OC} and power conversion efficiency (η_P) than treatment with BDT. However, changes in these properties do not explain the architecture-dependent performance of 1,2-BDT and 1,3-BDT-exchanged QDs. The difference in the energetic environment of the QD film between the np-HJ and SJ architectures suggests that a shift in the energy levels of the PbS QDs between the two different ligand treatments could explain this difference in performance.

In the SJ architecture, the interfacial energetics can be tuned in a controlled manner through modification of the electron- and hole-extracting contacts. A common modification to the simple ITO/PbS/cathode structure is to insert a layer of PEDOT:PSS as a hole-extracting layer between the ITO and the PbS QDs.[45,46] PEDOT:PSS is known to aid in hole injection into, and hole extraction out of, organic semiconductors with deep highest occupied molecular orbitals (HOMOs) as a result of its deep work function (E_F = 5.0 eV for PEDOT:PSS, *vs* 4.7 eV for ITO).[47,48] As shown in Figure 4a, the inclusion of a PEDOT:PSS hole-extracting layer results in a 3.2-fold improvement in η_P for a SJ photovoltaic fabricated with 1,3-BDT-exchanged PbS QDs, while it has a negligible effect on a 1,2-BDT-exchanged SJ photovoltaic. This observation matches what would be expected from the energy levels reported in

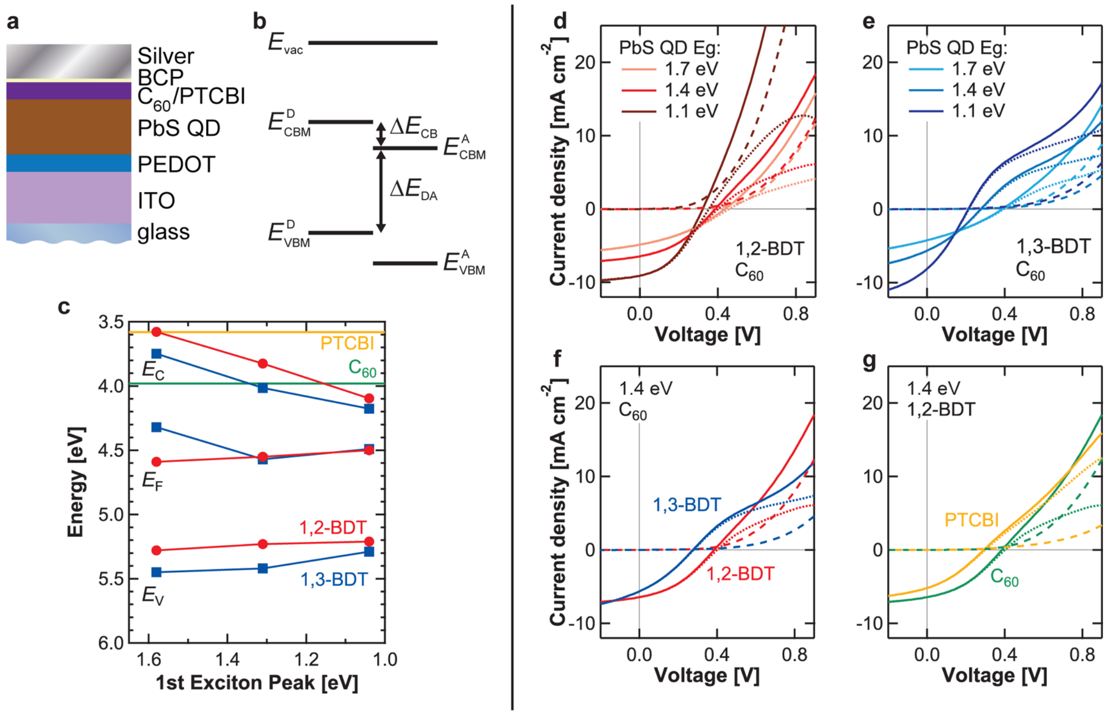

Figure 5. Ligand- and QD-size-induced changes in DA-HJ photovoltaic performance. (a) Device structure of the donor–acceptor heterojunction and (b) schematic band diagram of the donor–acceptor pair, showing a conduction band offset ΔE_{CB} that is favorable for photocurrent extraction. (c) Measured energy levels of three different sizes of PbS QDs, with LUMO energies of C_{60} and PTCBI from the literature. The conduction band energy E_C corresponds to the transport gap; the optical gap is omitted here for clarity. The experimental uncertainty of the QD energy levels determined by UPS is 0.1 eV; the uncertainty of the LUMOs of the organic materials determined by inverse photoelectron spectroscopy in the literature is 0.5 eV.[25] (d–g) Dark current (dashed curves), light current (solid curves), and photocurrent (dotted curves) of DA-HJ photovoltaics, comparing (d) 1,2-BDT-treated QDs of different size paired with C_{60}, (e) 1,3-BDT-treated QDs of different sizes paired with C_{60}, (f) 1,2-BDT and 1,3-BDT-treated QDs of a given size paired with C_{60}, and (g) 1,2-BDT-treated QDs paired with PTCBI and C_{60}.

Figure 1e: 1,3-BDT-treated QDs, with their deeper VBM, benefit more from the high-work-function PEDOT:PSS hole transport layer than do the 1,2-BDT-treated QDs.

Similarly, a thin layer of LiF is commonly inserted between the cathode and the electron transport layer in organic LEDs and solar cells, where it is shown to increase the efficiency of electron injection and extraction.[49,50] This effect is commonly attributed to a lowering of the effective cathode work function as a result of a strong interface dipole induced by the LiF, resulting in a reduced barrier height for electron injection.[51] In the PbS QD SJ architecture described here, a reduction in the cathode work function should result in a greater benefit for PbS QDs with a shallower VBM and CBM by strengthening the Schottky junction at the interface and increasing the driving force for electron extraction. Indeed, as shown in Figure 4b, the insertion of LiF results in a 2.2-fold improvement in η_P for 1,2-BDT-treated QDs but has a negligible effect on the η_P of 1,3-BDT-treated QDs, which is consistent with the shallower energy levels reported in Figure 1e for 1,2-BDT-treated PbS QDs.

The donor–acceptor heterojunction (DA-HJ) is an alternative to the SJ architecture that relies directly on the band offsets at the D–A interface (rather than on Schottky barrier formation, which is known to be sensitive to surface traps and other complications)[52] to separate charge carriers, thus providing an architecture wherein the interfacial energy level alignment can be probed more directly. Figure 5a displays a DA-HJ device architecture in which PbS QDs act as the electron donor and either buckminsterfullerene (C_{60}) or 3,4,9,10 perylenetetracarboxylic bisbenzimidazole (PTCBI) act as the electron acceptor.

Figure 5b displays an outline of the energy level structure in a DA-HJ photovoltaic device. An important design criterion for the DA-HJ is that ΔE_{CB}, given by $\Delta E_{CB} = E_{CBM}{}^{D} - E_{CBM}{}^{A}$, must be positive and sufficiently large to allow transfer of photogenerated electrons from the CBM of the donor to the lowest unoccupied molecular orbital (LUMO) of the acceptor. A large, positive ΔE_{CB} should also prevent unwanted back-transfer of photogenerated electrons from the acceptor to the donor. Thus, observing the performance of DA-HJ photovoltaic devices fabricated with different expected values of ΔE_{CB} enables shifts in the energy levels of the PbS QDs to be inferred and compared to those determined by UPS.

Figure 5c shows the measured energy levels of three different sizes of PbS QDs (λ = 725, 905, and

1153 nm first absorption peaks in solution) after ligand exchange with 1,2-BDT or 1,3-BDT. The CBM is found to change more with QD size than the VBM, as has been noted previously in the literature.[16,18] The LUMOs of C_{60} and PTCBI are taken from inverse photoelectron spectroscopy measurements reported in the literature to be 4.0 ± 0.5 and 3.6 ± 0.5 eV, respectively.[25] Figures 5d−g shows the dark current, light current, and photocurrent $J-V$ responses (J_{dark}, J_{light}, and J_{pc}, respectively, where $J_{pc} = J_{light} - J_{dark}$) of DA-HJ photovoltaics pairing these three different sizes of 1,2-BDT- and 1,3-BDT-exchanged PbS QDs with C_{60} and PTCBI.

As the bandgap of the 1,2-BDT-exchanged QDs is reduced, the reduced capacity for quasi-Fermi level splitting leads to a smaller V_{OC}, but the increased absorption at longer wavelengths leads to a higher J_{SC} (Figure 5d). This same trend is observed for 1,3-BDT-exchanged QDs (Figure 5e), but the diode properties for 1,3-BDT deviate substantially from ideal behavior. As the bandgap decreases and the CBM moves to deeper energies, J_{light} crosses J_{dark} at smaller voltages and a "kink" in the forward-bias J_{light} becomes more pronounced, corresponding to a reversal in the polarity of J_{pc} as the short circuit current (negative polarity) is subsumed by an increased photoconductivity (positive polarity). This increase in photoconductivity in forward bias is expected if the ΔE_{CB} at the donor−acceptor interface is made less positive, corresponding to a deepening of the donor CBM, as the barrier to electron transfer from acceptor to donor is reduced.

Similar trends are observed in Figure 5f,g when comparing the performance of PTCBI and C_{60} as acceptors and that of 1,2-BDT-exchanged QDs and 1,3-BDT-exchanged QDs as donors. The LUMO of PTCBI is ~0.4 eV shallower in energy than that of C_{60}, leading to a reduction in ΔE_{CB}; correspondingly, the DA-HJ employing PTCBI demonstrates a greater contribution from photoconductive back-electron transfer in the form of a lower-voltage $J_{light}-J_{dark}$ crossover. Similarly, from Figure 5c, the measured CBM of 1,3-BDT-exchanged 1.4 eV PbS QDs is 0.2 eV deeper than that of 1,2-BDT-exchanged PbS QDs of the same size, which also leads to a reduction in ΔE_{CB}; as such, J_{light} for 1,3-BDT demonstrates a stronger forward-bias "kink" and a lower-voltage crossover with J_{dark}.

Figure 5d−g shows that the substitution of 1,3-BDT for 1,2-BDT (which, from the energy level measurements reported here, results in a 0.1−0.2 eV deeper CBM) induces changes in DA-HJ photovoltaic performance that are qualitatively similar to those induced by reducing the bandgap of the QD or by substituting PTCBI for C_{60}, both of which are known from energy level measurements reported in the literature to result in a reduction in ΔE_{CB}. This observation provides support for the method of energy level measurement reported here and for the use of these energy levels in describing the performance of PbS QD optoelectronic devices.

CONCLUSION

In summary, the band energies of colloidal QDs can be modified by ligand exchange, resulting in energy level shifts of up to 0.9 eV for PbS QDs. Trends in energy level position between different ligands are confirmed by atomistic modeling, showing that the observed shifts result from contributions from both the QD-ligand interface dipole[14] and the intrinsic dipole moment of the ligand molecule itself.[27] These energy level shifts result in predictable changes in photovoltaic device operation and provide a guide to the optimal ligand choice and device architecture for QD photovoltaics. These findings have recently been employed to guide the design of a current-record-efficiency PbS QD photovoltaic device employing a cascaded energy level architecture.[22] These results identify ligand-induced band-energy shifts, in complement to quantum confinement-controlled bandgap modification, as a means of predictably controlling the electronic properties of colloidal QDs and as a critical adjustable parameter in the optimization of QD optoelectronic devices.

METHODS

PbS QD Synthesis and Film Preparation. All synthesis, fabrication, and testing are performed under oxygen- and water-free conditions unless otherwise stated. Oleic acid-capped PbS QDs are synthesized *via* standard literature methods[53] and purified three times by precipitation and centrifugation in a mixture of acetone and 1-butanol, followed by resuspension in hexane. After the final round of purification, the QDs are dissolved in octane at a concentration of 25 mg mL^{-1}. All solid QD films are prepared by sequential spin-casting. For each layer, ~15 μL of QD solution is dispensed through a 0.02 μm filter (Anotop) onto a 12.5 mm × 12.5 mm substrate and spin-cast at 1500 rpm for 15 s. Roughly 200 μL of ligand solution is then dispensed through a 0.1 μm filter (PTFE) onto the substrate, allowed to sit for 30 s, and spun dry. The substrate is then flooded with the solvent used for ligand exchange and spun dry three times to remove unbound ligand, and the entire process is repeated; each complete iteration results in the deposition of ~20 nm of QDs. The ligand concentrations and solvents used in this study are representative of well-characterized ligand exchange conditions from the literature: benzenethiol and 1,2-, 1,3-, and 1,4-benzenedithiol, 1.7 mM in acetonitrile (ACN);[54] 1,2-ethanedithiol, 1.7 mM in ACN;[42] 3-mercaptopropionic acid, 115 mM in methanol (MeOH);[6] ethylenediamine, 1 M in MeOH;[55] ammonium thiocyanate, 30 mM in MeOH;[7] and tetrabutylammonium fluoride, chloride, bromide, and iodide, 30 mM in MeOH.[56] All chemicals are purchased from Sigma-Aldrich at the highest purity available.

Ultraviolet Photoelecton Spectroscopy. UPS spectra are collected using an Omicron ultrahigh vacuum system with a base pressure of 10^{-10} mbar. The substrates for the UPS measurement are 12.5 mm × 12.5 mm glass slides coated with

Cr(10 nm)/Au(100 nm) anodes by thermal evaporation and stored in air-free conditions without further surface treatment. Five sequential spin-casting cycles of PbS QDs with various ligand treatments, performed as described above, result in a QD film thickness of ∼100 nm. Electrical contact from the steel sample plate to the Cr/Au anode is made using carbon tape. Samples for UPS are transported from an inert-atmosphere glovebox (<1 ppm of O_2) to the UPS system without exposure to air using a load-locked transfer system. During the UPS measurement, illumination at 21.22 eV is provided by the He(I) emission line from a helium discharge lamp, and the chamber pressure increases to 10^{-7} mbar. The samples are biased at −5.0 V to ensure accurate determination of the low-kinetic energy cutoff, and electron emission is collected at 0° from normal. Single kinetic energy scans are completed in <45 s to minimize charging. Cutoff energies are determined from the intersection of a linear extrapolation of the cutoff region to a linear extrapolation of the baseline.

Density Functional Theory Calculations. DFT calculations are performed using the Vienna Ab Initio Simulation Packages (VASP)[57] with the generalized gradient approximation of Perdew−Burke−Ernzerhof (PBE)[58] for the exchange and correlation functional. The projector-augmented-wave method is adopted to describe the core electrons. Our recent work has shown that variations in ligand coverage density can significantly affect electronic properties;[13] surface coverage here is held constant at one binding atom per surface lead atom. An energy cutoff of 400 eV and a Monkhorst−Pack *k*-point sampling of 5 × 5 × 1 are used after extensive convergence analyses. A large vacuum spacing of >20 Å is used to prevent inter-slab interactions. Each (100) PbS slab consists of 8 single layers, and pseudohydrogen atoms with fractional charges of 5/3 and 1/3e are chosen to passivate the surface Pb and S atoms on the back layer. Ligands and the top five layers of the PbS slab are fully relaxed using the conjugate gradient method until the structure satisfies the following relaxation criteria: (i) the energy difference between two consecutive ionic steps is less than 10^{-4} eV, and (ii) the maximum Hellmann−Feynman forces acting on each atom are less than 0.02 eV Å^{-1}. Dipole corrections are included to remove the spurious electrostatic interactions between neighboring supercells.

Photovoltaic Device Fabrication. Photovoltaic devices are deposited onto ITO-coated glass substrates (Thin Film Devices) that have been cleaned by ultrasonication in micro-90 soap solution, deionized water, acetone, and 2-propanol, followed by treatment with ozone plasma. The device area is defined by the anode−cathode overlap to be 1.24 mm^2. Zinc oxide (Plasmaterials) is deposited by rf-sputtering as described in ref 43. Molybdenum oxide (99.9995%), lithium fluoride (99.99%), buckminsterfullerene (C_{60}), 3,4,9,10 perylenetetracarboxylic bisbenzimidazole (PTCBI), bathocuproine (BCP), aluminum, silver, and gold are deposited by thermal evaporation at 0.5−1 Å/s at a base pressure of 10^{-6} Torr. Polyethylenedioxythiophene−polystyrene sulfonate (PEDOT:PSS, conductive grade, Sigma-Aldrich) is deposited by spin-casting in air at 4000 rpm for 60 s, then annealed at 150 °C inside a nitrogen-atmosphere glovebox for 30 min. Where noted in the text, the ITO-coated glass substrates are soaked overnight in a solution of 12 mM (3-mercaptopropyl)trimethoxysilane (3-MPTMS) in toluene to increase QD adhesion to the substrate, then sonicated for 1 min in 2-propanol to remove unbound 3-MPTMS. Np-heterojunction (np-HJ) photovoltaic devices utilize the architecture ITO/ZnO (50 nm)/PbS QD (160 nm)/MoO_3 (10 nm)/Au (100 nm). Schottky junction photovoltaic devices utilize the architecture ITO/PEDOT:PSS/PbS QD (160 nm)/LiF (0.7 nm)/Al (100 nm) unless otherwise noted. Donor−acceptor photovoltaic devices utilize the architecture ITO/PEDOT:PSS/PbS QD (160 nm)/(C_{60} or PTCBI) (40 nm)/BCP (10 nm)/Ag (100 nm).

Electrical Characterization. Current density−voltage (*J*−*V*) curves of photovoltaic devices are recorded using a Keithley 6487 picoammeter, and 100 mW cm^2 illumination is provided by a xenon lamp (Newport 96000) equipped with an AM1.5G filter. Spectral mismatch and additional electrical characterization details are reported in the Supporting Information.

Conflict of Interest: The authors declare no competing financial interest.

Acknowledgment. The authors thank M. Baldo for use of the ultraviolet photoelectron spectroscopy system and the National Energy Research Scientific Computing Center for computing resources. P.R.B. thanks J. Jean, D. D. Wanger, T. L. Andrew, T. P. Osedach, N. J. Thompson, and P. Jadhav for insightful discussions. P.R.B. acknowledges support from the Fannie and John Hertz Foundation and the National Science Foundation, and D.K. acknowledges support from the Samsung Scholarship Foundation. This work is partially supported by the Samsung Advanced Institute of Technology.

Supporting Information Available: Ultraviolet photoelectron spectra and absorption spectra of QD-ligand complexes. Ligand binding simulations on Pb-rich PbS(111) surface, monodentate and bidentate ligand binding simulations on PbS(100) surface, and double-sided ligand binding simulations on PbS(100) slab. Field-effect mobility, recombination rate, and density of states of ligand-exchanged PbS QDs, and solar cell spectral mismatch. This material is available free of charge *via* the Internet at http://pubs.acs.org.

REFERENCES AND NOTES

1. Kim, J. Y.; Voznyy, O.; Zhitomirsky, D.; Sargent, E. H. 25th Anniversary Article: Colloidal Quantum Dot Materials and Devices: A Quarter-Century of Advances. *Adv. Mater.* **2013**, *25*, 4986–5010.
2. Gao, J.; Luther, J. M.; Semonin, O. E.; Ellingson, R. J.; Nozik, A. J.; Beard, M. C. Quantum Dot Size Dependent J-V Characteristics in Heterojunction ZnO/PbS Quantum Dot Solar Cells. *Nano Lett.* **2011**, *11*, 1002–1008.
3. Talapin, D. V.; Murray, C. B. PbSe Nanocrystal Solids for N- and P-Channel Thin Film Field-Effect Transistors. *Science* **2005**, *310*, 86–89.
4. Ip, A. H.; Thon, S. M.; Hoogland, S.; Voznyy, O.; Zhitomirsky, D.; Debnath, R.; Levina, L.; Rollny, L. R.; Carey, G. H.; Fischer, A.; *et al.* Hybrid Passivated Colloidal Quantum Dot Solids. *Nat. Nanotechnol.* **2012**, *7*, 577–582.
5. Klem, E. J. D.; MacNeil, D. D.; Cyr, P. W.; Levina, L.; Sargent, E. H. Efficient Solution-Processed Infrared Photovoltaic Cells: Planarized All-Inorganic Bulk Heterojunction Devices *via* Inter-Quantum-Dot Bridging During Growth from Solution. *Appl. Phys. Lett.* **2007**, *90*, 183113.
6. Pattantyus-Abraham, A. G.; Kramer, I. J.; Barkhouse, A. R.; Wang, X.; Konstantatos, G.; Debnath, R.; Levina, L.; Raabe, I.; Nazeeruddin, M. K.; Grätzel, M.; *et al.* Depleted-Heterojunction Colloidal Quantum Dot Solar Cells. *ACS Nano* **2010**, *4*, 3374–3380.
7. Fafarman, A. T.; Koh, W.; Diroll, B. T.; Kim, D. K.; Ko, D.-K.; Oh, S. J.; Ye, X.; Doan-Nguyen, V.; Crump, M. R.; Reifsnyder, D. C.; *et al.* Thiocyanate-Capped Nanocrystal Colloids: Vibrational Reporter of Surface Chemistry and Solution-Based Route to Enhanced Coupling in Nanocrystal Solids. *J. Am. Chem. Soc.* **2011**, *133*, 15753–15761.
8. Tang, J.; Kemp, K. W.; Hoogland, S.; Jeong, K. S.; Liu, H.; Levina, L.; Furukawa, M.; Wang, X.; Debnath, R.; Cha, D.; *et al.* Colloidal-Quantum-Dot Photovoltaics Using Atomic-Ligand Passivation. *Nat. Mater.* **2011**, *10*, 765–771.
9. Choi, J. J.; Bealing, C. R.; Bian, K.; Hughes, K. J.; Zhang, W.; Smilgies, D.-M.; Hennig, R. G.; Engstrom, J. R.; Hanrath, T. Controlling Nanocrystal Superlattice Symmetry and Shape-Anisotropic Interactions Through Variable Ligand Surface Coverage. *J. Am. Chem. Soc.* **2011**, *133*, 3131–3138.
10. Liu, Y.; Gibbs, M.; Puthussery, J.; Gaik, S.; Ihly, R.; Hillhouse, H. W.; Law, M. Dependence of Carrier Mobility on Nanocrystal Size and Ligand Length in PbSe Nanocrystal Solids. *Nano Lett.* **2010**, *10*, 1960–1969.
11. Voznyy, O.; Zhitomirsky, D.; Stadler, P.; Ning, Z.; Hoogland, S.; Sargent, E. H. A Charge-Orbital Balance Picture of Doping in Colloidal Quantum Dot Solids. *ACS Nano* **2012**, *6*, 8448–8455.

12. Oh, S. J.; Berry, N. E.; Choi, J.-H.; Gaulding, E. A.; Paik, T.; Hong, S.-H.; Murray, C. B.; Kagan, C. R. Stoichiometric Control of Lead Chalcogenide Nanocrystal Solids to Enhance Their Electronic and Optoelectronic Device Performance. *ACS Nano* **2013**, *7*, 2413–2421.
13. Kim, D.; Kim, D.-H.; Lee, J.-H.; Grossman, J. C. Impact of Stoichiometry on the Electronic Structure of PbS Quantum Dots. *Phys. Rev. Lett.* **2013**, *110*, 196802.
14. Soreni-Harari, M.; Yaacobi-Gross, N.; Steiner, D.; Aharoni, A.; Banin, U.; Millo, O.; Tessler, N. Tuning Energetic Levels in Nanocrystal Quantum Dots through Surface Manipulations. *Nano Lett.* **2008**, *8*, 678–684.
15. Timp, B. A.; Zhu, X.-Y. Electronic Energy Alignment at the PbSe Quantum Dots/ZnO($10\bar{1}0$) Interface. *Surf. Sci.* **2010**, *604*, 1335–1341.
16. Jasieniak, J.; Califano, M.; Watkins, S. E. Size-Dependent Valence and Conduction Band-Edge Energies of Semiconductor Nanocrystals. *ACS Nano* **2011**, *5*, 5888–5902.
17. Munro, A. M.; Zacher, B.; Graham, A.; Armstrong, N. R. Photoemission Spectroscopy of Tethered CdSe Nanocrystals: Shifts in Ionization Potential and Local Vacuum Level as a Function of Nanocrystal Capping Ligand. *ACS Appl. Mater. Interfaces* **2010**, *2*, 863–869.
18. Hyun, B.-R.; Zhong, Y.-W.; Bartnik, A. C.; Sun, L.; Abruña, H. D.; Wise, F. W.; Goodreau, J. D.; Matthews, J. R.; Leslie, T. M.; Borrelli, N. F. Electron Injection from Colloidal PbS Quantum Dots into Titanium Dioxide Nanoparticles. *ACS Nano* **2008**, *2*, 2206–2212.
19. Gao, J.; Perkins, C. L.; Luther, J. M.; Hanna, M. C.; Chen, H.-Y.; Semonin, O. E.; Nozik, A. J.; Ellingson, R. J.; Beard, M. C. N-Type Transition Metal Oxide as a Hole Extraction Layer in PbS Quantum Dot Solar Cells. *Nano Lett.* **2011**, *11*, 3263–3266.
20. Yuan, M.; Zhitomirsky, D.; Adinolfi, V.; Voznyy, O.; Kemp, K. W.; Ning, Z.; Lan, X.; Xu, J.; Kim, J. Y.; Dong, H.; *et al.* Doping Control *via* Molecularly Engineered Surface Ligand Coordination. *Adv. Mater.* **2013**, *25*, 5586–5592.
21. Katsiev, K.; Ip, A. H.; Fischer, A.; Tanabe, I.; Zhang, X.; Kirmani, A. R.; Voznyy, O.; Rollny, L. R.; Chou, K. W.; Thon, S. M.; *et al.* The Complete In-Gap Electronic Structure of Colloidal Quantum Dot Solids and Its Correlation with Electronic Transport and Photovoltaic Performance. *Adv. Mater.* **2014**, *26*, 937–942.
22. Chuang, C.-H. M.; Brown, P. R.; Bulović, V.; Bawendi, M. G. Improved Performance and Stability in Quantum Dot Solar Cells through Band Alignment Engineering. *Nat. Mater.* **2014**, DOI: 10.1038/nmat3984.
23. Brus, L. Electronic Wave Functions in Semiconductor Clusters: Experiment and Theory. *J. Phys. Chem.* **1986**, *90*, 2555–2560.
24. Dalven, R. Electronic Structure of PbS, PbSe, and PbTe. *Solid State Phys.* **1974**, *28*, 179–224.
25. Hwang, J.; Wan, A.; Kahn, A. Energetics of Metal–Organic Interfaces: New Experiments and Assessment of the Field. *Mater. Sci. Eng. R Reports* **2009**, *64*, 1–31.
26. Zhou, Y.; Fuentes-Hernandez, C.; Shim, J.; Meyer, J.; Giordano, A. J.; Li, H.; Winget, P.; Papadopoulos, T.; Cheun, H.; Kim, J.; *et al.* A Universal Method To Produce Low-Work Function Electrodes for Organic Electronics. *Science* **2012**, *336*, 327–332.
27. Heimel, G.; Romaner, L.; Zojer, E.; Brédas, J.-L. Toward Control of the Metal-Organic Interfacial Electronic Structure in Molecular Electronics: A First-Principles Study on Self-Assembled Monolayers of Pi-Conjugated Molecules on Noble Metals. *Nano Lett.* **2007**, *7*, 932–940.
28. Yang, S.; Prendergast, D.; Neaton, J. B. Tuning Semiconductor Band Edge Energies for Solar Photocatalysis *via* Surface Ligand Passivation. *Nano Lett.* **2012**, *12*, 383–388.
29. Cho, K.-S.; Talapin, D. V.; Gaschler, W.; Murray, C. B. Designing PbSe Nanowires and Nanorings Through Oriented Attachment of Nanoparticles. *J. Am. Chem. Soc.* **2005**, *127*, 7140–7147.
30. Bealing, C. R.; Baumgardner, W. J.; Choi, J. J.; Hanrath, T.; Hennig, R. G. Predicting Nanocrystal Shape Through Consideration of Surface-Ligand Interactions. *ACS Nano* **2012**, *6*, 2118–2127.
31. Luther, J. M.; Law, M.; Song, Q.; Perkins, C. L.; Beard, M. C.; Nozik, A. J. Structural, Optical, and Electrical Properties of Self-Assembled Films of PbSe Nanocrystals Treated with 1,2-Ethanedithiol. *ACS Nano* **2008**, *2*, 271–280.
32. Tang, J.; Brzozowski, L.; Barkhouse, D. A. R.; Wang, X.; Debnath, R.; Wolowiec, R.; Palmiano, E.; Levina, L.; Pattantyus-Abraham, A. G.; Jamakosmanovic, D.; *et al.* Quantum Dot Photovoltaics in the Extreme Quantum Confinement Regime: The Surface-Chemical Origins of Exceptional Air- and Light-Stability. *ACS Nano* **2010**, *4*, 869–878.
33. Koh, W.-K.; Saudari, S. R.; Fafarman, A. T.; Kagan, C. R.; Murray, C. B. Thiocyanate-Capped PbS Nanocubes: Ambipolar Transport Enables Quantum Dot Based Circuits on a Flexible Substrate. *Nano Lett.* **2011**, *11*, 4764–4767.
34. Law, M.; Luther, J. M.; Song, Q.; Hughes, B. K.; Perkins, C. L.; Nozik, A. J. Structural, Optical, and Electrical Properties of PbSe Nanocrystal Solids Treated Thermally or with Simple Amines. *J. Am. Chem. Soc.* **2008**, *130*, 5974–5985.
35. Yaacobi-Gross, N.; Garphunkin, N.; Solomeshch, O.; Vaneski, A.; Susha, A. S.; Rogach, A. L.; Tessler, N. Combining Ligand-Induced Quantum- Confined Stark Effect with Type II Heterojunction Bilayer Structure in CdTe and CdSe Nanocrystal-Based Solar Cells. *ACS Nano* **2012**, *6*, 3128–3133.
36. Yaacobi-Gross, N.; Soreni-Harari, M.; Zimin, M.; Kababya, S.; Schmidt, A.; Tessler, N. Molecular Control of Quantum-Dot Internal Electric Field and Its Application to CdSe-Based Solar Cells. *Nat. Mater.* **2011**, *10*, 974–979.
37. Zehner, R. W.; Parsons, B. F.; Hsung, R. P.; Sita, L. R. Tuning the Work Function of Gold with Self-Assembled Monolayers Derived from X-[C_6H_4-C≡C-]$_n$$C_6H_4$-SH ($n = 0, 1, 2$; X = H, F, CH_3, CF_3, and OCH_3). *Langmuir* **1999**, *15*, 1121–1127.
38. Alloway, D. M.; Hofmann, M.; Smith, D. L.; Gruhn, N. E.; Graham, A. L.; Colorado, R., Jr.; Wysocki, V. H.; Lee, T. R.; Lee, P. A.; Armstrong, N. R. Interface Dipoles Arising from Self-Assembled Monolayers on Gold: UV–Photoemission Studies of Alkanethiols and Partially Fluorinated Alkanethiols. *J. Phys. Chem. B* **2003**, *107*, 11690–11699.
39. de Boer, B.; Hadipour, A.; Mandoc, M. M.; van Woudenbergh, T.; Blom, P. W. M. Tuning of Metal Work Functions with Self-Assembled Monolayers. *Adv. Mater.* **2005**, *17*, 621–625.
40. Leschkies, K. S.; Beatty, T. J.; Kang, M. S.; Norris, D. J.; Aydil, E. S. Solar Cells Based on Junctions Between Colloidal PbSe Nanocrystals and Thin ZnO Films. *ACS Nano* **2009**, *3*, 3638–8648.
41. Johnston, K. W.; Pattantyus-Abraham, A. G.; Clifford, J. P.; Myrskog, S. H.; MacNeil, D. D.; Levina, L.; Sargent, E. H. Schottky-Quantum Dot Photovoltaics for Efficient Infrared Power Conversion. *Appl. Phys. Lett.* **2008**, *92*, 151115.
42. Zhao, N.; Osedach, T. P.; Chang, L.-Y.; Geyer, S. M.; Wanger, D.; Binda, M. T.; Arango, A. C.; Bawendi, M. G.; Bulović, V. Colloidal PbS Quantum Dot Solar Cells with High Fill Factor. *ACS Nano* **2010**, *4*, 3743–3752.
43. Brown, P. R.; Lunt, R. R.; Zhao, N.; Osedach, T. P.; Wanger, D. D.; Chang, L.-Y.; Bawendi, M. G.; Bulović, V. Improved Current Extraction from ZnO/PbS Quantum Dot Heterojunction Photovoltaics Using a MoO_3 Interfacial Layer. *Nano Lett.* **2011**, *11*, 2955–2961.
44. Jeong, K. S.; Tang, J.; Liu, H.; Kim, J.; Schaefer, A. W.; Kemp, K.; Levina, L.; Wang, X.; Hoogland, S.; Debnath, R.; *et al.* Enhanced Mobility-Lifetime Products in PbS Colloidal Quantum Dot Photovoltaics. *ACS Nano* **2012**, *6*, 89–99.
45. Ma, W.; Swisher, S. L.; Ewers, T.; Engel, J.; Ferry, V. E.; Atwater, H. A.; Alivisatos, A. P. Photovoltaic Performance of Ultrasmall PbSe Quantum Dots. *ACS Nano* **2011**, *5*, 8140–8147.
46. Choi, J. J.; Lim, Y.-F.; Santiago-Berrios, M. B.; Oh, M.; Hyun, B.-R.; Sun, L.; Bartnik, A. C.; Goedhart, A.; Malliaras, G. G.; Abruña, H. D.; *et al.* PbSe Nanocrystal Excitonic Solar Cells. *Nano Lett.* **2009**, *9*, 3749–3755.
47. Koch, N.; Kahn, A.; Ghijsen, J.; Pireaux, J.-J.; Schwartz, J.; Johnson, R. L.; Elschner, A. Conjugated Organic Molecules on Metal *versus* Polymer Electrodes: Demonstration of a

Key Energy Level Alignment Mechanism. *Appl. Phys. Lett.* **2003**, *82*, 70–72.

48. Milliron, D. J.; Hill, I. G.; Shen, C.; Kahn, A.; Schwartz, J. Surface Oxidation Activates Indium Tin Oxide for Hole Injection. *J. Appl. Phys.* **2000**, *87*, 572–576.
49. Shaheen, S. E.; Jabbour, G. E.; Morrell, M. M.; Kawabe, Y.; Kippelen, B.; Peyghambarian, N.; Nabor, M.-F.; Schlaf, R.; Mash, E. A.; Armstrong, N. R. Bright Blue Organic Light-Emitting Diode with Improved Color Purity Using a LiF/Al Cathode. *J. Appl. Phys.* **1998**, *84*, 2324–2327.
50. Tang, J.; Wang, X.; Brzozowski, L.; Barkhouse, D. A. R.; Debnath, R.; Levina, L.; Sargent, E. H. Schottky Quantum Dot Solar Cells Stable in Air under Solar Illumination. *Adv. Mater.* **2010**, *22*, 1398–1402.
51. Brabec, C. J.; Shaheen, S. E.; Winder, C.; Sariciftci, N. S.; Denk, P. Effect of LiF/Metal Electrodes on the Performance of Plastic Solar Cells. *Appl. Phys. Lett.* **2002**, *80*, 1288–1290.
52. Luther, J. M.; Law, M.; Beard, M. C.; Song, Q.; Reese, M. O.; Ellingson, R. J.; Nozik, A. J. Schottky Solar Cells Based on Colloidal Nanocrystal Films. *Nano Lett.* **2008**, *8*, 3488–3492.
53. Chang, L.-Y.; Lunt, R. R.; Brown, P. R.; Bulović, V.; Bawendi, M. G. Low-Temperature Solution-Processed Solar Cells Based on PbS Colloidal Quantum Dot/CdS Heterojunctions. *Nano Lett.* **2013**, *13*, 994–999.
54. Koleilat, G. I.; Levina, L.; Shukla, H.; Myrskog, S. H.; Hinds, S.; Pattantyus-Abraham, A. G.; Sargent, E. H. Efficient, Stable Infrared Photovoltaics Based on Solution-Cast Colloidal Quantum Dots. *ACS Nano* **2008**, *2*, 833–840.
55. Talgorn, E.; Gao, Y.; Aerts, M.; Kunneman, L. T.; Schins, J. M.; Savenije, T. J.; van Huis, M. A.; van der Zant, H. S. J.; Houtepen, A. J.; Siebbeles, L. D. A. Unity Quantum Yield of Photogenerated Charges and Band-like Transport in Quantum-Dot Solids. *Nat. Nanotechnol.* **2011**, *6*, 733–739.
56. Zhitomirsky, D.; Furukawa, M.; Tang, J.; Stadler, P.; Hoogland, S.; Voznyy, O.; Liu, H.; Sargent, E. H. N-Type Colloidal-Quantum-Dot Solids for Photovoltaics. *Adv. Mater.* **2012**, *24*, 6181–6185.
57. Kresse, G.; Furthmüller, J. Efficiency of Ab-Initio Total Energy Calculations for Metals and Semiconductors Using a Plane-Wave Basis Set. *Comput. Mater. Sci.* **1996**, *6*, 15–50.
58. Perdew, J.; Burke, K.; Ernzerhof, M. Generalized Gradient Approximation Made Simple. *Phys. Rev. Lett.* **1996**, *77*, 3865–3868.